*J. Fluid Mech.* (1987), *vol.* 178, *pp.* 303–323
*Printed in Great Britain*

# Vortex shedding behind a square cylinder in transonic flows

By TAKEO NAKAGAWA†

Max-Planck-Institut für Strömungsforschung, D-3400 Göttingen, Böttingerstrasse 4–8,
Federal Republic of Germany

(Received 19 July 1986)

This paper is primarily concerned with Mach-number effects on the vortex shedding behind a square cylinder (side length $D = 20$ mm) in a Reynolds-number range of $0.696 \times 10^5 < Re < 4.137 \times 10^5$, and a Mach-number range of $0.1522 < M < 0.9049$.

Regular periodic vortex shedding is present, irrespective of the appearance of shock waves around a square cylinder. The shape of the vortices is, however, deformed by the shock waves, and each vortex centre becomes non-uniform while the vortex passes through the gap between the upper and lower shock waves. Weak shock waves around the square cylinder do not alter the Strouhal number, but strong shock waves weaken the vortex shedding and increase the Strouhal number suddenly. Acoustic waves have been recorded by the Mach–Zehnder interferometer when the Mach number is close to the critical value. The acoustic waves are generated most strongly at the instant when each vortex hits the foot of the shock waves formed above and below the vortex formation region.

From the present work and that of Okajima (1982), it is suggested that the Strouhal number of alternating vortices shed from a square cylinder can be estimated to be about 0.13 in the Reynolds-number range between $10^2$ and $3.4 \times 10^5$.

## 1. Introduction

The Kármán vortex street is observable downstream of Aeolian wires (Rayleigh 1915), struts of airplanes, radio and television towers, various antennas, power lines, flame stabilizers and fuel sprays, for example. Thus, its applicability is quite wide and important. It is particularly significant if Kármán vortex streets induce flutter (or galloping) and resonance in these structures.

Regarding the origin of the Kármán vortex street, however, neither stability theories (Kármán 1911, 1912) nor phenomenological models (Mallock 1907; Bénard 1908) give any sound information so far. The mechanism leading to the formation of the vortices and to the subsequent shedding has been only qualitatively explained. However, there do exist some important suggestions on the formation mechanism of alternating vortices. Gerrard (1966), for example, has proposed that the entrainment of fluid from the interior of the formation region and its replenishment by reverse flow is fundamental to the determination of a scale which determines the frequency of vortex shedding. Very recently, Nakagawa (1986) has investigated the flow around a circular cylinder, and has concluded that the asymmetry of the vortex

---

† Present address: Department of Mechanical System Engineering, Kanazawa Institute of Technology, Nonoichi, Kanazawa 921, Japan.

pair and the unstable system of three vortices in the vortex formation region leads to the alternating vortex shedding.

It is fairly well known how the vortex shedding behind a two-dimensional circular cylinder depends upon the Reynolds number (e.g. Roshko 1961; Ericsson & Reding 1979). On the other hand, less information on the question of how the vortex shedding behind a two-dimensional square cylinder depends upon the Reynolds number is available. However, some results on flows around a square cylinder in a uniform flow have been reported (e.g. Bearman & Trueman 1972; Lee 1975; Okajima 1982; Nakamura & Ohya 1986). In the case of a square cylinder, where the separation points are fixed at the leading edges, the aerodynamic characteristics are considered to be relatively insensitive to the Reynolds number. At extremely low Reynolds number, flow around a square cylinder is known to separate at the trailing edges rather than the leading edges, for the separation at the leading edges is indiscernible owing to the immediate reattachment on the side surfaces. With an increase of the Reynolds number, the flow separation at the leading edges develops, and the steady reattachment on the side surfaces becomes impossible (Okajima 1982).

How the vortex shedding from a bluff body depends on the Mach number has been reported by Naumann & Pfeiffer (1958), Thomann (1959), Nash, Quincey & Callinan (1963), Dyment (1982) and others. Naumann & Pfeiffer (1958) have reported that the critical Mach number, at which local supersonic areas around a circular cylinder appear in the flow, does not influence the Strouhal number, and that the periodic vortex generation can be observed even in the case where the shock waves due to local supersonic areas reach from wall to wall in the wind tunnel. Thomann (1959) has shown that in subsonic flow the vortex street appears in the wake of a circular cylinder and a wedge, but it disappears gradually in the transonic region. However, for higher Mach numbers, 1.8 and 3, no vortex streets have been observed. Variation of the Strouhal number with the Mach number for a blunt-trailing-edge model has been reported by Nash *et al.* (1963). At Mach numbers up to 0.9 the Strouhal number remains constant at a value of about 0.25. The development of trailing shock waves behind the model is marked by a progressive increase in the Strouhal number to about 0.31. The arrival of the shock waves at the trailing edge of the model and the establishment of supersonic flow over the afterbody is not observed to bring about an immediate suppression of the periodic effects. At Mach numbers above 0.975, the vortex street is observed to be less strong, but the Strouhal number is then in the region of 0.4, and falls only slowly with increase of the Mach number. Dyment (1982) has proposed that change of the Strouhal number at high transonic Mach numbers can be explained by the coupling between the vortex street and the vortex formation region, and the degree of the coupling is determined by the shock waves interrupting it.

This paper is primarily concerned with experiments on the vortex shedding behind a square cylinder (side length $D = 20$ mm) in a Reynolds-number range of $0.696 \times 10^5 < Re < 4.137 \times 10^5$, and a Mach-number range of $0.1522 < M < 0.9049$, which covers almost the whole range of transonic Mach number. The main purpose of the present study is to clarify how the Mach number influences the vortex shedding behind the square cylinder, especially when shock waves appear in the local flow field.

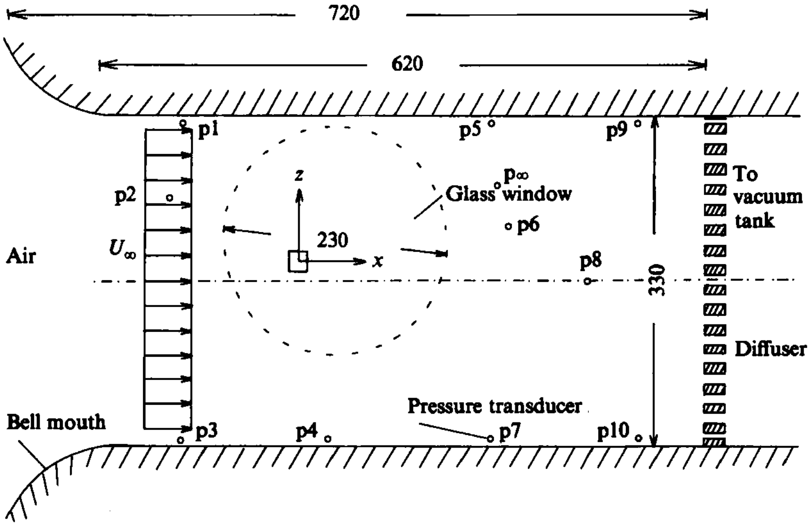

FIGURE 1. Schematic diagram of the experiment (units, mm).

## 2. Experiment

Figure 1 shows a schematic diagram of the experiment. The test-section of the transonic wind tunnel is 620 mm long × 330 mm high × 100 mm wide. Air is sucked from the laboratory and then flows into a vacuum tank of 130 $m^3$ through the test-section. The velocity in the test-section is controlled by adjusting the openings of the diffuser.

Two square cylinders are used for the generation of periodic vortices. One cylinder of side length $D = 20$ mm has aspect ratio of 5, while the other cylinder of side length $D = 4$ mm has aspect ratio of 25. Each square cylinder is installed between the two transparent glass windows. The windows have a diameter of 230 mm and are of interferometric quality.

A Mach–Zehnder interferometer (Zeiss) has been used for high-speed flow visualization. This optical method is based on the principle of interference, and provides directly the density field averaged across the working section (Liepmann & Roshko 1957). When the air flow is steady and isentropic (so that viscous effects are neglected), the density ratio $\tilde{\rho}$ of the local density to stagnation density is related to the pressure ratio $\tilde{p}$ of the local pressure to stagnation pressure by the expression

$$\tilde{p} = \tilde{\rho}^{\gamma}, \tag{1}$$

where $\gamma$ is the ratio of specific heats, and is 1.401 for dry air at a temperature of 15 °C and atmospheric pressure. When the test-section is in vacuum, the interferogram shows a total of 96 fringes in this optical arrangement, where each fringe is shown as either a white line or black line. The density ratio $\tilde{\rho}$ on each interferogram in the present optical arrangement is given by the relation

$$\tilde{\rho} = 1 - 0.01058N, \tag{2}$$

where $N$ is the number of the fringe order starting from 0 either at a white line or black line including the stagnation point. It is, therefore, possible to obtain the

| Transducer | Coordinate<br>$x$ (mm) | <br>$y$ (mm) | <br>$z$ (mm) |
|---|---|---|---|
| p1 | −125 | 50 | 140 |
| p2 | −135 | 50 | 65 |
| p3 | −125 | 50 | −180 |
| p4 | 30 | 50 | −180 |
| p5 | 195 | 50 | 140 |
| p6 | 215 | 50 | 35 |
| p7 | 195 | 50 | −180 |
| p8 | 295 | 50 | −20 |
| p9 | 345 | 50 | 140 |
| p10 | 345 | 50 | −180 |
| $p_\infty$ | 205 | 50 | 35 |

TABLE 1. Positions of pressure transducers

| Experiment no. | $U_\infty$ (m/s) | $f$ (Hz) | $St = Df/U_\infty$ | $Re = DU_\infty/\nu$ | $M = U_\infty/c$ |
|---|---|---|---|---|---|
| 1 | 52.2 | 351 | 0.1345 | $0.696\times10^5$ | 0.1522 |
| 2 | 77.6 | 527 | 0.1358 | $1.035\times10^5$ | 0.2263 |
| 3 | 103.3 | 664 | 0.1286 | $1.377\times10^5$ | 0.3013 |
| 4 | 129.0 | 821 | 0.1273 | $1.720\times10^5$ | 0.3762 |
| 5 | 155.8 | 977 | 0.1254 | $2.077\times10^5$ | 0.4544 |
| 6 | 184.6 | 1231 | 0.1334 | $2.461\times10^5$ | 0.5383 |
| 7 | 216.6 | 1485 | 0.1371 | $2.888\times10^5$ | 0.6317 |
| 8 | 256.7 | 1661 | 0.1294 | $3.423\times10^5$ | 0.7486 |
| 9 | 280.7 | 2404 | 0.1713 | $3.743\times10^5$ | 0.8186 |
| 10 | 310.3 | 2834 | 0.1827 | $4.137\times10^5$ | 0.9049 |
| 11 | 129.0 | 4301 | 0.1334 | $0.344\times10^5$ | 0.3762 |

TABLE 2. Summary of experiments

pressure ratio, averaged across the working section at any point in the flow, simply by counting the number of the fringe order $N$ on the interferogram and then substituting the density ratio (2) into (1). Note that the accuracy of the pressure measured is independent of total numbers of the fringes. High-speed recordings of the interferogram have been made at a film frame rate of about 7 kHz using a rotating drum camera.

High-sensitivity pressure transducers YCS (Kulite) have been used for pressure measurement in the test-section. A total of 10 pressure transducers are fixed at positions p1–p10 on the side wall, as shown in figure 1, and these positions are listed in table 1, where a right-handed coordinate system of axes, $x$, $y$ and $z$ is used and the origin of the coordinates is at the centre of the cylinder. The sensor of the pressure transducer has a circular membrane of 6 mm diameter, and the natural frequency is 100 kHz. A static pressure transducer DPI 200 (NATEC) has been used for calibrating the free-stream velocity $U_\infty$ without the square cylinder and for monitoring the pressure in the test-section during the experiment. The position $p_\infty$ of the static pressure transducer is also listed in table 1, and the interface of the static pressure transducer is an IEC-11S (Digital Equipment).

The computer used for the experiment is a PDP-11/34 (Digital Equipment) with a connected array processor AP-120B (Floating Point Systems). The controller CA11-FP (Digital Equipment) is the interface for a 16-channel transient recorder (Le Croy), the real-time clock and digital input/output port. Each of the transient recorder channels has 8 K storage capacity of 10 bit pressure data at any sampling frequency up to 1 MHz. In this experiment, the transient recorder has been used for recording 8 K data at a sampling frequency of 20 kHz. The data analyses have been done with the array processor, which is capable of performing the fast Fourier transformation of 1024 data within 3 ms.

The main parameter in the present experiment is the Mach number, although the Reynolds number varies with it. A total of 11 experiments have been conducted and are summarized in table 2, where the 20 mm square cylinder is used for experiments 1–10, and the 4 mm square cylinder is used only for experiment 11.

## 3. Results

### 3.1. *High-speed flow visualization*

Figure 2 shows the high-speed flow visualization of the vortex shedding behind the square cylinder in experiment 3. The sequence of events begins at $t = 1$ and continues to $t = 6$. The time increment $\Delta t$ between adjacent frames and the non-dimensional time increment $\Delta \tilde{t} = U_\infty \Delta t/D$ are 148 μs and 0.764, respectively. The Mach number is 0.3013, which is well below the critical value of about 0.74, and thus no local flow areas are supersonic yet. It can be observed in figure 2 that the flow separates at the leading edges, the vortex shedding shows high periodicity and regularity, and each of the vortices is well defined.

Figure 3 shows the high-speed flow visualization of the vortex shedding behind the square cylinder in experiment 4. The sequence of events begins at $t = 5$ and continues to $t = 8$. In these interferograms, the ratio of the local pressure to stagnation pressure $\tilde{p}$ is inscribed at 5 fringe intervals and at each vortex centre. When one notes the vortex just behind the lower trailing edge of the square cylinder, the pressure ratio $\tilde{p}$ decreases from $t = 5$ to $t = 7$, and starts increasing from $t = 7$. Now, it will be shown how the pressure ratio $\tilde{p}$ at the vortex centre behind the upper trailing edge varies with time. At $t = 5$, the vortex is about to be shed from the vortex formation region. The pressure ratio $\tilde{p}$ decreases from $t = 5$ to $t = 6$, but it increases from $t = 6$ to $t = 8$, at which the pressure ratio $\tilde{p}$ becomes 0.80. It is, therefore, considered that the pressure ratio at the vortex centre repeatedly, increases and decreases. At $t = 6$, the pressure ratio at the vortex centre near the lower trailing edge is 0.64, which is smaller than the pressure ratio of 0.66 at the vortex centre behind it. The pressure ratio increases as one moves around the trailing edge. However, the pressure ratio again decreases as the wake axis is approached in the middle of the vortex formation region. Then, the pressure ratio again increases until the vortex arrives at the end of the vortex formation region. Furthermore, during the pinching-off process of the vortex, the pressure ratio decreases. Then, the pressure ratio increases and approaches an almost constant value with increasing distance from the vortex formation region.

Figure 4 shows the loci of the vortex positions in experiment 4. The sequence of events begins at $t = 4$ and continues to $t = 10$. In this figure, the boundary of the vortex formation region at $t = 2$ is delineated with the one-point chain line, whereas the adjacent vortices are connected by the dotted line. The loci of the upper and lower main vortices get close to each other once in the middle of the vortex formation region, and then become almost parallel further downstream.

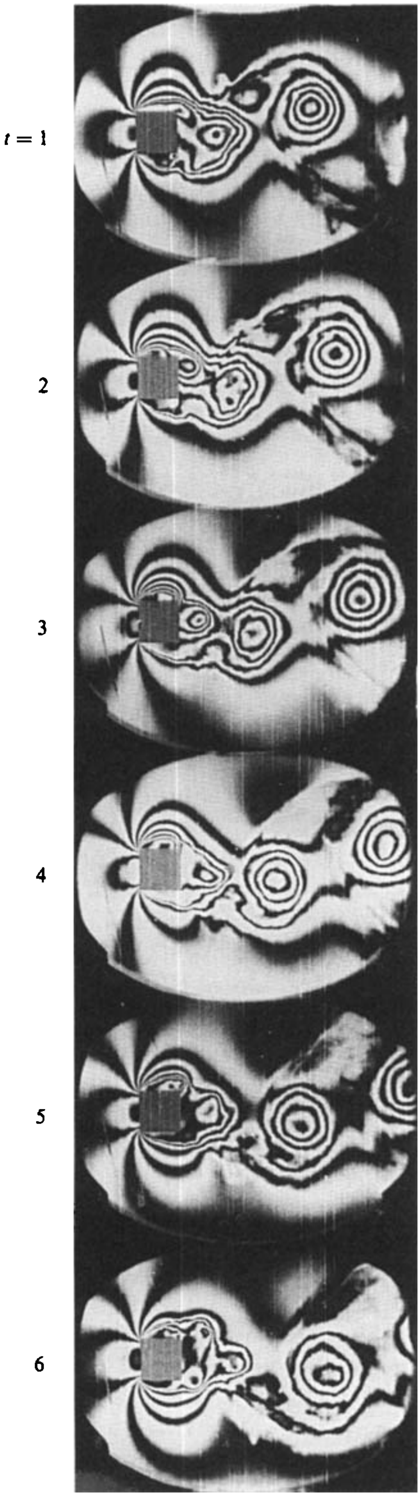

FIGURE 2. High-speed flow visualization of the vortex shedding behind the square cylinder in experiment 3. $\Delta t = 148\ \mu s$, $\Delta \bar{t} = 0.764$, $U_\infty = 103.3$ m/s, $f = 664$ Hz, $St = 0.1286$, $Re = 1.377 \times 10^5$, $M = 0.3013$.

Figure 5 shows the high-speed flow visualization of the vortex shedding behind the square cylinder in experiment 8. The sequence of events begins at $t = 1$ and continues to $t = 6$. The Mach number in this experiment is very close to the critical value of about 0.74, at which shock waves are formed in the local flow region. It must be noted that there exist several acoustic waves propagating in the upstream direction in each frame, for the propagation speed $(c-u)$ of the acoustic waves must be very small in this case, where $c$ is the sound speed and $u$ the local flow velocity. This is the primary reason why acoustic waves are recorded only in this experiment, while no acoustic waves are recorded in the other experiments. One could differentiate between an acoustic wave and a shock wave in figure 5, for the former wave propagates upstream, but the latter wave is stationary. At this Mach number, shock waves are formed at the upper and lower sides of the vortex formation region (see figure 6 for more detail). It may be interesting to note that the acoustic wave is generated most strongly at the instant when the vortex hits the foot of the shock wave. Another important point which must be mentioned on figure 5 is that each vortex centre becomes non-uniform while the vortex passes through the gap between the upper and lower shock waves. Then, the vortex is shed into the highly irregular pressure field behind the gap. It may be evident that this diffusion of the vortex is mainly caused by the interaction between the vortex and shock wave, and the shock waves limit the coupling between the vortex street and the vortex formation region. However, the periodicity and regularity of the vortex-shedding process are still preserved, although the shape of the vortices is deformed in comparison with that in experiment 3 (see figure 2).

Figure 6 shows an enlarged interferogram (or frame) at $t = 5$ for the high-speed flow visualization presented in figure 5. In this figure, the ratio of the local pressure to stagnation pressure $\tilde{p}$ is inscribed at five fringe intervals and at each vortex centre. Acoustic waves and shock waves identified in figure 5 can be seen around the vortex formation region. This figure indicates how the pressure field behind the gap between the upper and lower shock waves is irregular: the shed vortex with the pressure ratio of 0.35 at the centre is surrounded by many smaller vortices, which are irregular in shape.

Figure 7 shows the high-speed flow visualization of the vortex shedding behind the square cylinder in experiment 10. The sequence of events begins at $t = 1$ and continues to $t = 6$. The Mach number is 0.9049, which is well above the critical value, and thus the local flow areas around the square cylinder and the vortex formation region are supersonic. Strong shock waves normal to the wake axis are formed at the downstream end of the vortex formation region. The vortices are generated in the vortex formation region, shed downstream alternately, and then pass through the gap between the upper and lower shock waves. It may be noteworthy that the vortex shedding at this high Mach number is still periodic and regular, and the vortex-shedding frequency is the largest among all the present experiments (see figure 10), although the spectral-peak frequency itself takes a small value of 215 Hz. The origin of this low spectral-peak frequency will be discussed in §4. Since the coupling between the vortex street and the vortex formation region is severely limited by the shock waves at this stage, the vortex shedding becomes the weakest, and the shape of the vortices is highly deformed. The pressure field behind the gap between the upper and lower shock waves is again highly irregular.

### 3.2. *Pressure measurements*

Figure 8 illustrates how the pressure spectrum $S$ depends upon the frequency $f$ in experiment 7, and shows that all the spectral-peak frequencies recorded by the

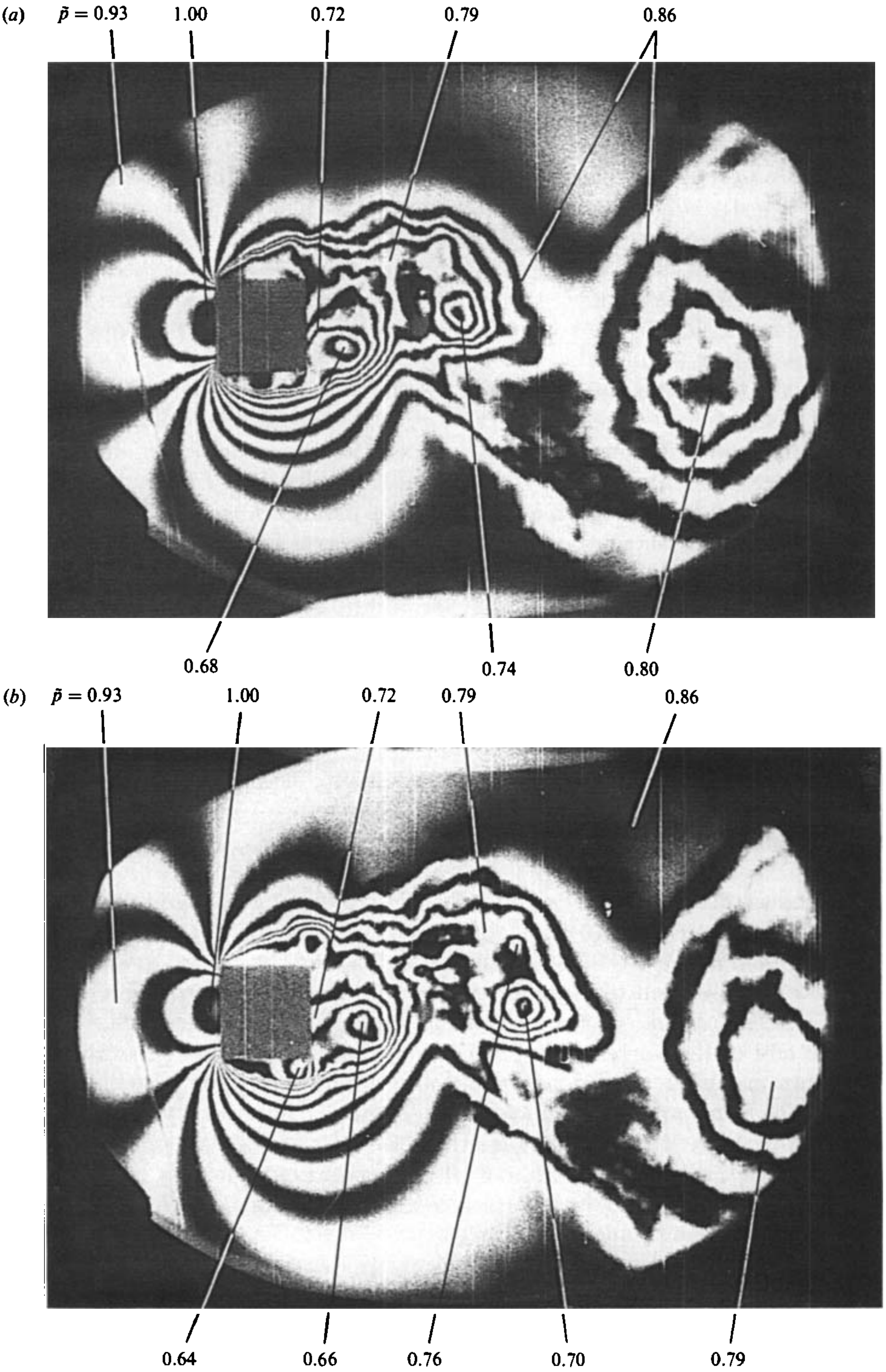

FIGURE 3$(a, b)$. For caption see facing page.

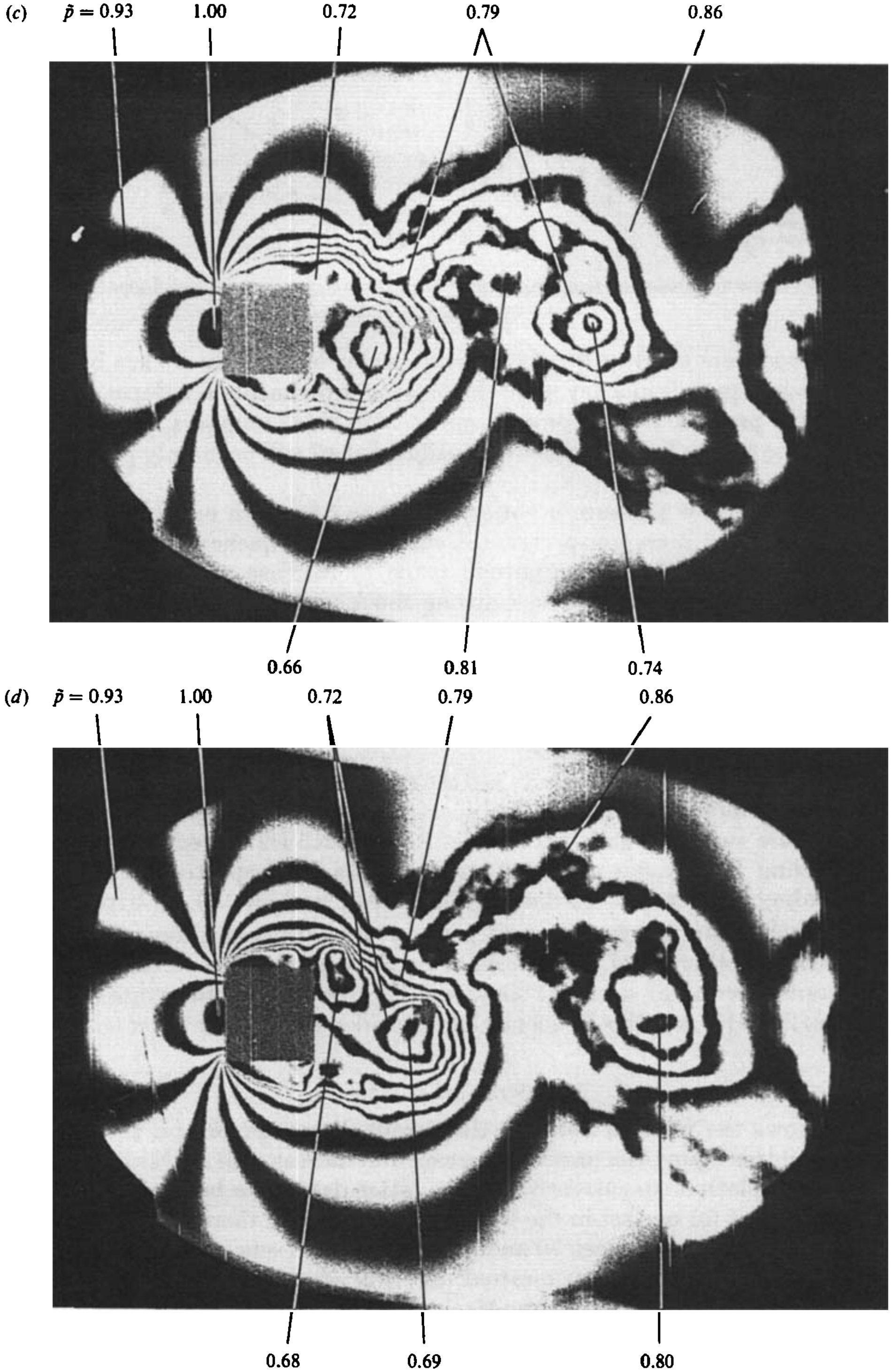

**Figure 3.** High-speed flow visualization of the vortex shedding behind the square cylinder in experiment 4. $\Delta t$ = 145 μs, $\Delta \tilde{t} = 0.935$, $U_\infty$ = 129.0 m/s, $f$ = 821 Hz, $St = 0.1273$, $Re = 1.720 \times 10^6$, $M = 0.3762$. (*a*) $t = 5$; (*b*) $t = 6$; (*c*) $t = 7$; (*d*) $t = 8$.

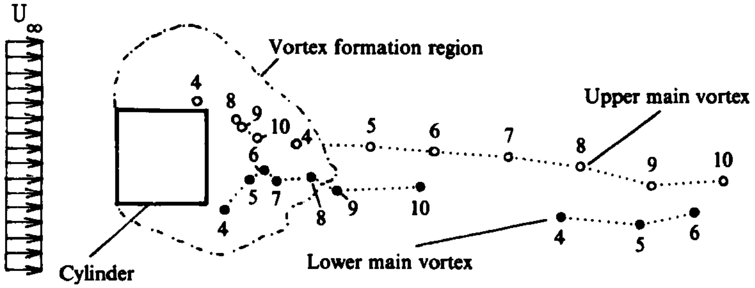

FIGURE 4. Loci of the vortices shed from the square cylinder in experiment 4. See figure 3 for legends.

pressure transducers at p1–p10 take the same value of 1485 Hz. It has been found that the spectral-peak frequency in all the present experiments is independent of the position of the pressure transducers, except at high Mach numbers, so that for each experiment the results for the pressure transducer at p7 will be mainly presented and discussed.

Figure 9 shows how pressure $p$ varies with time $t$ for each experiment, whereas figure 10 shows how pressure spectrum $S$ varies with frequency $f$. It can be noted in figure 9 that the pressure amplitude tends to increase with increasing Mach number, but suddenly decreases once strong shock waves appear in experiments 9 and 10. Figure 9 also indicates that the frequency of the pressure fluctuations increases with increasing Mach number. However, in each of experiments 1–8 the pressure record is composed essentially of a single notable frequency component, while in experiments 9 and 10 the higher-frequency components are superimposed on the lower-frequency components.

Figure 10 shows that in experiments 1–8 the spectral-peak frequency increases with increasing Mach number. However, the spectral peak frequencies in experiments 9 and 10 decrease suddenly and become 234 Hz and 215 Hz respectively, while the vortex-shedding frequencies are 2404 Hz and 2834 Hz respectively, where each vortex-shedding frequency is marked with an arrow in figure 10. In experiment 9, the pressure spectrum shows a second peak at the vortex-shedding frequency of 2404 Hz. On the other hand, in experiment 10, the pressure spectrum due to the pressure transducer at p7 does not show any notable peak at the vortex-shedding frequency of 2834 Hz, but this frequency has been identified by the other transducers.

### 3.3. *Strouhal number*

Figure 11 shows the relation between the Strouhal number *St* and the Reynolds number *Re*. In this figure, the present experimental data as well as Okajima's (1982) data have been plotted concurrently. All the latter data have been obtained in the wind tunnel except for one set in the water tank. This plot, therefore, covers a wide Reynolds-number range between 70 and $3.423 \times 10^5$. Two sets of data in the present experiments 9 and 10 have been omitted, for it is considered that these Strouhal numbers are primarily governed by the Mach number, but not the Reynolds number. The Strouhal number is about 0.10 at the Reynolds number of 70. The Strouhal number increases with increasing Reynolds number and attains a maximum value of about 0.15 at $Re \approx 200$. Then the Strouhal number decreases with increasing Reynolds number and takes a minimum value of about 0.12 at $Re \approx 10^3$. With further increase of the Reynolds number, the Strouhal number increases gradually, and

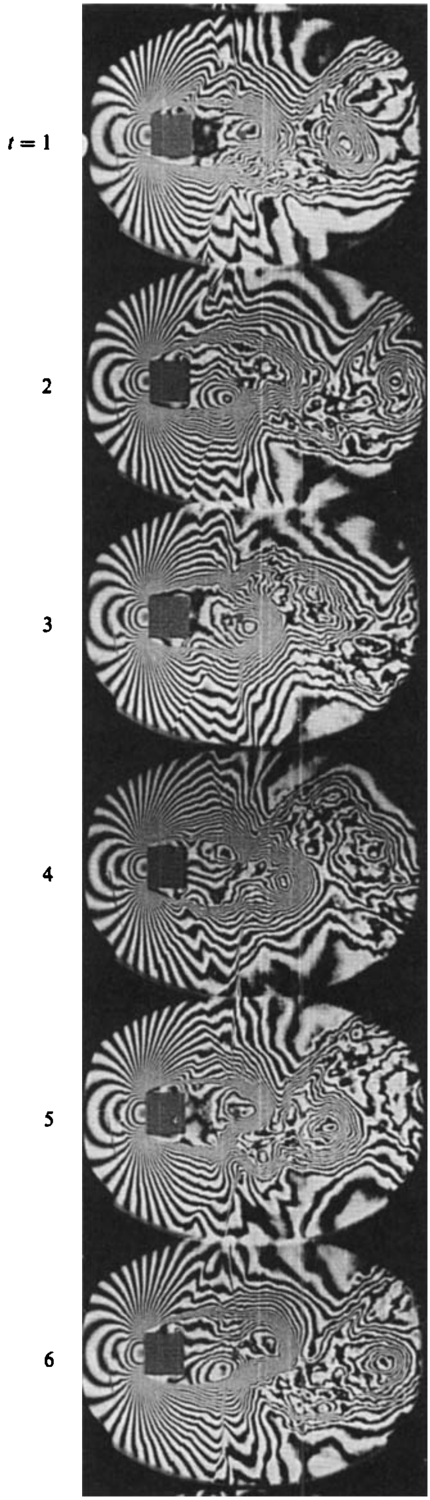

FIGURE 5. High-speed flow visualization of the vortex shedding behind the square cylinder in experiment 8. $\Delta t = 145\ \mu\mathrm{s}$, $\Delta \tilde{t} = 1.861$, $U_\infty = 256.7$ m/s, $f = 1661$ Hz, $St = 0.1294$, $Re = 3.423 \times 10^5$, $M = 0.7486$.

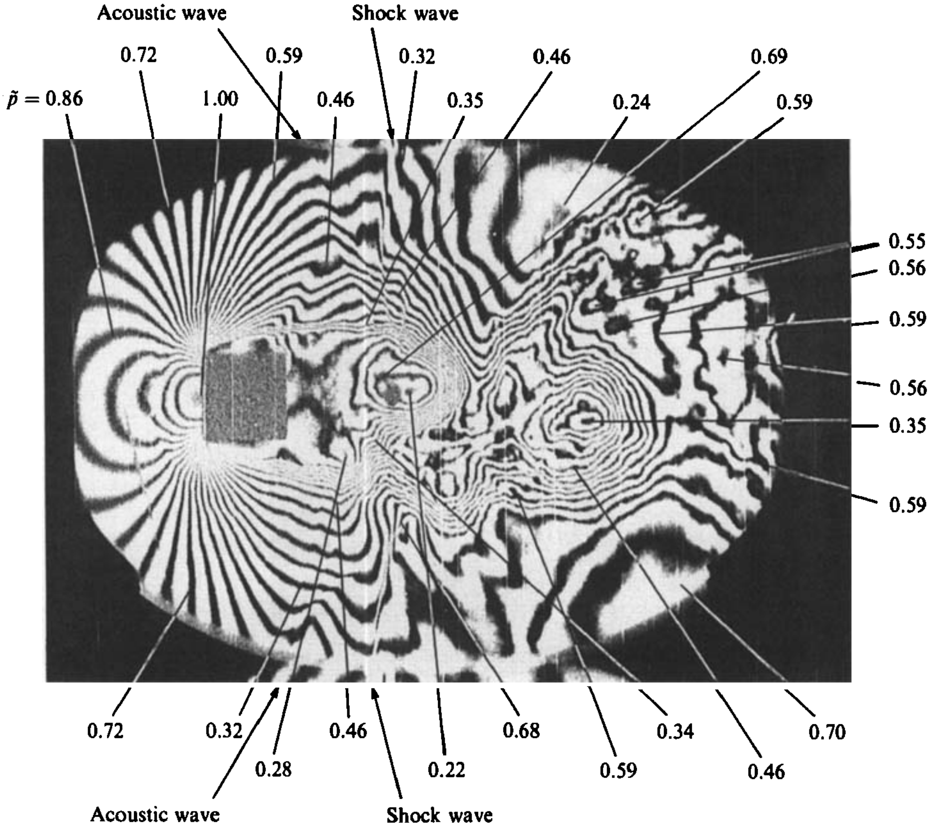

FIGURE 6. An enlarged interferogram at $t = 5$ for the high-speed flow visualization presented in figure 5. See figure 5 for legends.

reaches the value of about 0.13 at $Re \approx 10^4$. However, the Strouhal number becomes almost independent of the Reynolds number once it exceeds this value. It is, therefore, suggested that one could estimate the Strouhal number of a square cylinder as 0.13 in this Reynolds-number range. This information may be quite valuable from the engineering point of view.

Figure 12 shows an interferogram visualizing the flow around the 4 mm square cylinder. As already stated in §2, the 4 mm square cylinder gives an aspect-ratio of 25, so that it may warrant two-dimensionality of the flow, whereas the aspect ratio of the 20 mm square cylinder is only 5. However, in the case of the present experimental arrangement, the effect of the aspect ratio on the Strouhal number is not discernible in figure 11. In figure 12, the ratio of the local pressure to stagnation pressure $\tilde{p}$ has been inscribed at several points. The pressure ratio in the vortex formation region is 0.74. However, the pressure ratio increases and becomes 0.84 just behind the vortex formation region, but does not change essentially with increase of distance from it. This suggests that although the vortex is diffused and weakened through the vortex-shedding process, it survives for a fairly long time and distance after being shed from the vortex formation region. It is also notable in this figure that the vortex spacing is not uniform. For example, the transverse spacing between the loci of the upper and lower main vortices increases with increasing distance from the vortex formation region. The non-uniformity of the vortex spacing may be due

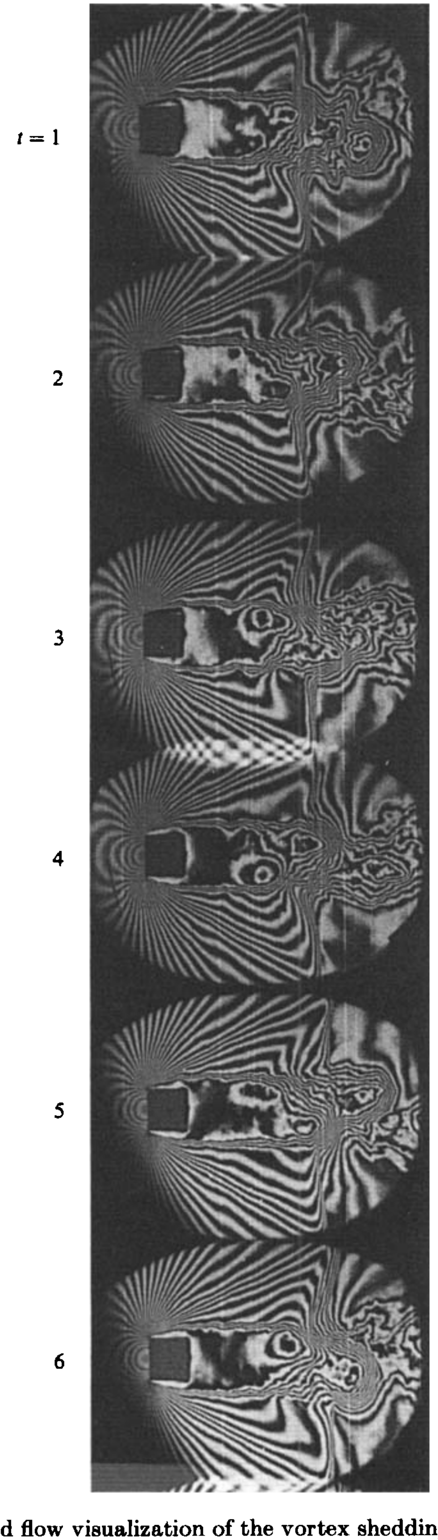

FIGURE 7. High-speed flow visualization of the vortex shedding behind the square cylinder in experiment 10. $\Delta t = 147$ μs, $\Delta \bar{t} = 2.281$, $U_\infty = 310.3$ m/s, $Re = 4.137 \times 10^5$, $M = 0.9049$.

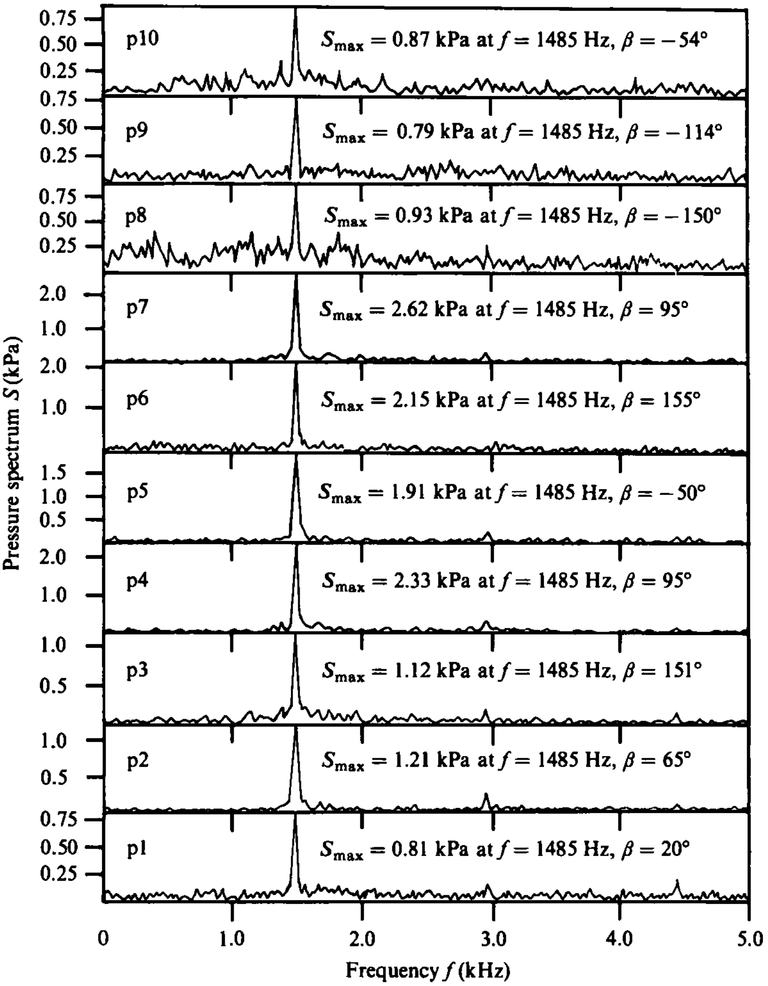

FIGURE 8. Pressure spectrum $S$ *vs.* frequency $f$ in experiment 7.

to the compressibility of the flow leading to the diffusion of the vortices, but not due to the non-two-dimensionality of the flow, if one considers the relatively high aspect ratio of 25 in this case.

Figure 13 shows the relation between the Strouhal number $St$ and the Mach number $M$. This figure shows that at Mach numbers up to 0.7486, which is greater than the critical Mach number, the Strouhal number remains constant at a value of about 0.13, but at Mach number 0.8186 the Strouhal number jumps to the value of 0.1713 and then becomes 0.1817 at Mach number 0.9049.

## 4. Discussion

High-speed flow-visualization pictures shown in figures 5 and 7, as well as the pressure records shown in figures 9 and 10, have clearly shown that regular periodic vortex shedding is still present, irrespective of the appearance of the strong shock waves on the upper and lower sides of the vortex formation region. However, once

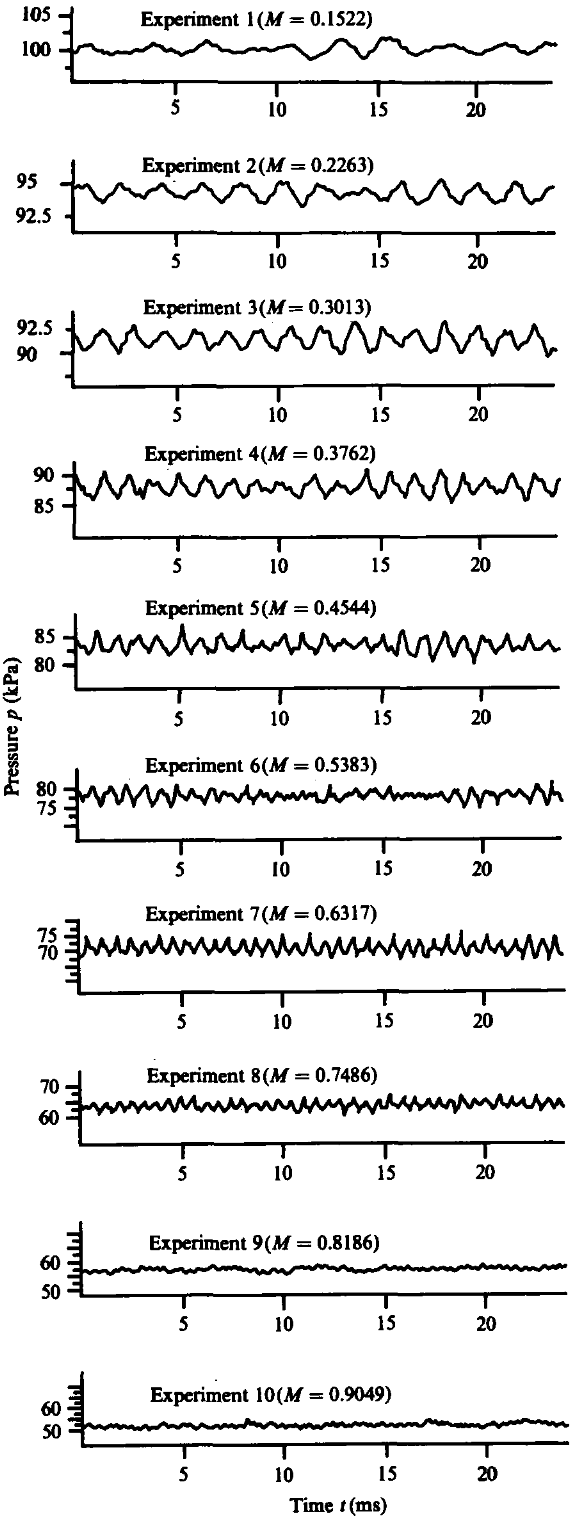

FIGURE 9. Pressure *vs*. time $t$ for each experiment.

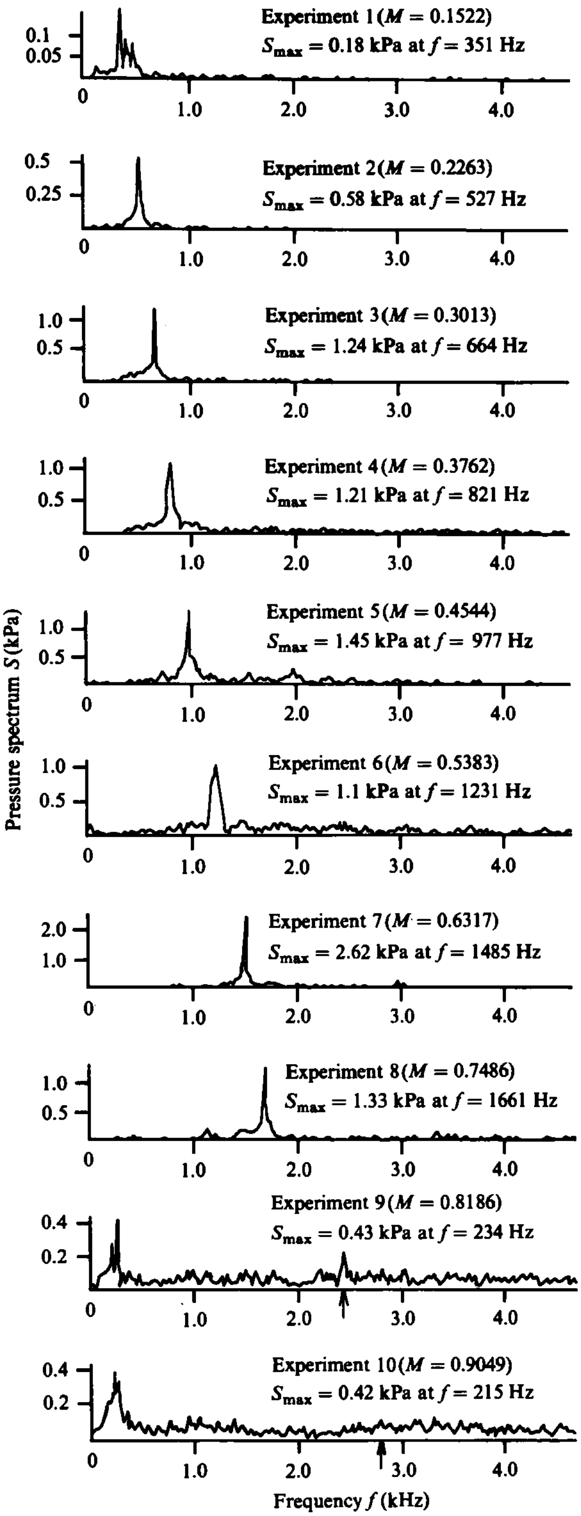

FIGURE 10. Pressure spectrum $S$ *vs.* frequency $f$ for each experiment.

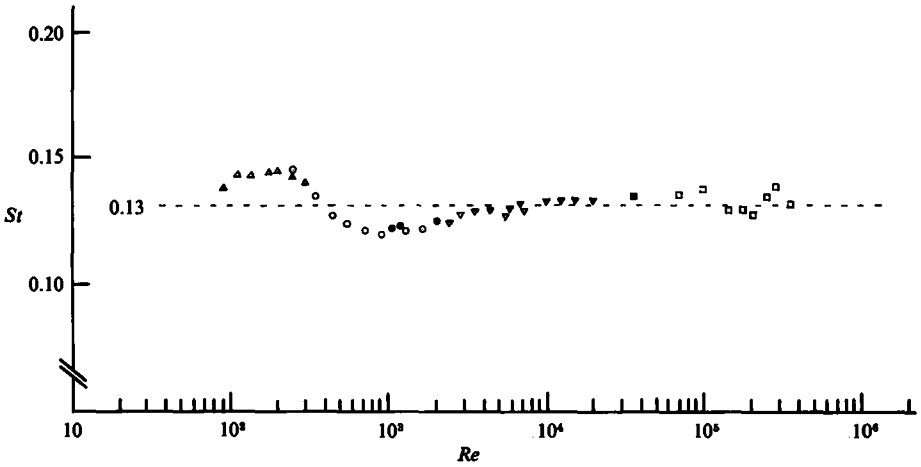

FIGURE 11. Strouhal number $St$ *vs.* Reynolds number $Re$. Present experiment: □, $H = 20$ mm; ■, $H = 4$ mm. Okajima's (1982) data: ○, $H = 2$ mm; ●, $H = 4$ mm; ▽, $H = 8$ mm; △, $H = 8$ mm (water tank); ▼, $H = 15$ mm.

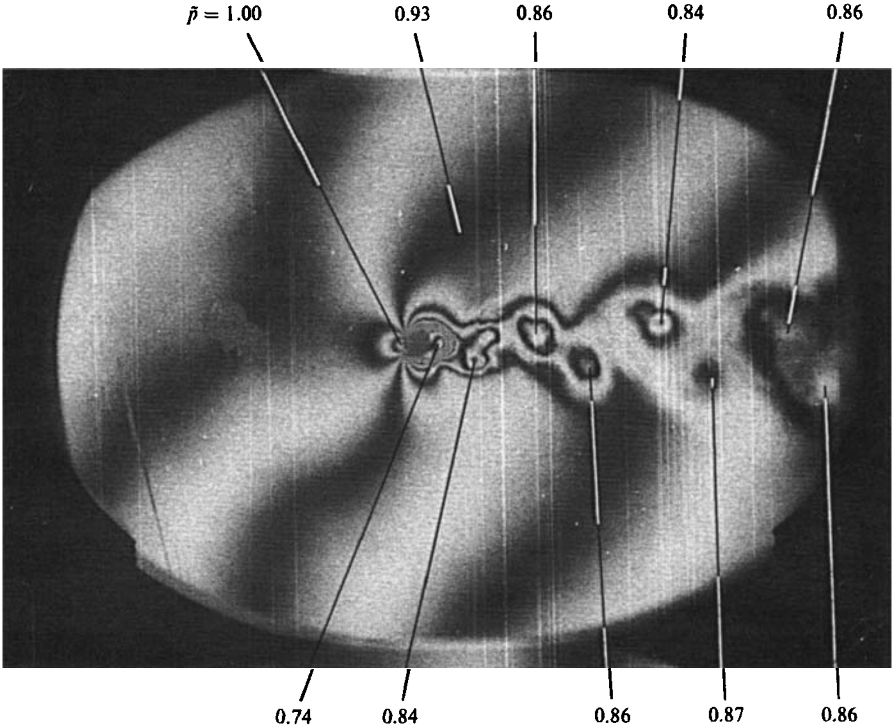

FIGURE 12. Interferogram visualizing the flow around small square cylinder ($D = 4$ mm). $U_\infty = 129.0$ m/s, $f = 4301$ Hz, $St = 0.1334$, $Re = 0.344 \times 10^5$, $M = 0.3762$.

strong shock waves appear, the spectral-peak frequency itself decreases suddenly, as seen in the pressure spectra for experiments 9 and 10 in figure 10. It is considered that this may be caused by strong shock waves that inhibit the upstream propagation of the pressure disturbances.

It is suggested here that, when the shock waves are formed, a feedback oscillation

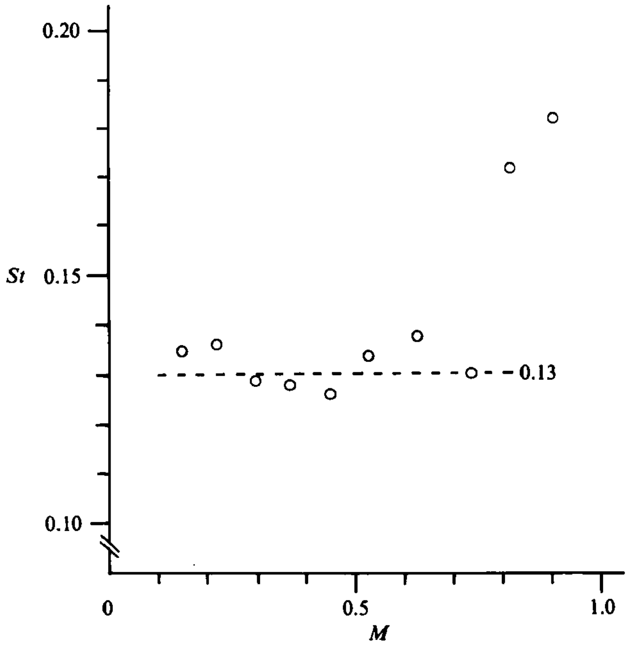

FIGURE 13. Strouhal number *St vs.* Mach number *M*.

is induced in the space between the shock front and the downstream diffuser in the test-section, in which a disturbance generates an acoustic pulse that propagates upstream, reflects and then regenerates the disturbance. It may be clear that the frequency of the oscillation is not given by a simple measure of distance and sound speed, for in its upstream travel the time required is $L/(c-u)$ and downstream is $L/(c+u)$, where $L$ is the distance in which the feedback oscillation is generated, $c$ the sound speed and $u$ the flow velocity. Thus, the oscillation period $T$ and oscillation frequency $f$ are given, respectively, by

$$T = \frac{2Lc}{c^2-u^2},$$

and

$$f = \frac{c^2-u^2}{2Lc}.$$

It may be worth noting that the oscillation frequency can become rather low as the flow velocity $u$ approaches the sound speed $c$. Finite geometry of the test-section may also induce other acoustic oscillations characterized by those scales. For example, such oscillations may be generated between the upper and lower walls or between the sidewalls. It is, however, clear that these acoustic waves would be generated without the shock waves, so that they must have no relevance to the low-frequency spectral peaks recorded in experiments 9 and 10.

The frequency of the suggested feedback oscillation has been estimated in terms of the above relation, and is compared with the present measurement, where the flow velocity $u$ is assumed to equal the free-stream velocity $U_\infty$. Results of this comparison are summarized in table 3, where the distance $L$ between the shock wave and the diffuser, flow velocity $u$ (or free-stream velocity $U_\infty$) and sound speed $c$ are the values in the present experiment. Table 3 shows that the estimated frequency decreases with

| | $M = 0.8186$ | $M = 0.9049$ |
|---|---|---|
| Distance between shock wave and diffuser $L$(m) | 0.345 | 0.3417 |
| Flow velocity $u$(= free stream velocity $U_\infty$) (m/s) | 280.7 | 310.3 |
| Sound speed $c$(m/s) | 342.9 | 342.9 |
| Estimated frequency of feedback oscillation $fe$(Hz) | 164 | 91 |
| Measured frequency of feedback oscillation $fm$(Hz) | 234 | 215 |

TABLE 3. Summary of the feedback oscillation frequencies

increasing Mach number. Note the frequency thus estimated can be zero when the free-stream velocity is equal to the sound speed. This means that the feedback oscillation can take any small frequency. When $M = 0.8186$, the spectral peak appears at $f = 234$ Hz, which may be compared with the estimated frequency of 164 Hz. On the other hand, when $M = 0.9049$, the spectral-peak frequency of 215 Hz may be compared with the estimated frequency of 91 Hz.

However, it must be stressed that the present estimation of the frequency for the feedback oscillation between the strong shock and the diffuser must remain only qualitative. For first, the flow velocity $u$ is tentatively assumed to be equal to the free-stream velocity $U_\infty$, though these two velocities may be different from each other. Secondly, reflection conditions at the shock wave and at the diffuser have not been taken into consideration. It is evident that the reflection conditions depend upon the detailed properties of the shock wave and the diffuser, which are hard to estimate in general. The quantitative estimation of the frequency for the feedback oscillation has been considered to be beyond the scope of the present paper.

Thomann (1959) has shown that in subsonic flow the vortex street appears in the wake of a circular cylinder, but it disappears gradually in the transonic region. However, for higher Mach numbers, 1.8 and 3, no vortex streets have been observed. It is suggested here that this is caused by the shock wave, which cuts off the downstream wake from the formation region. At this stage, the shock wave forms a thin dense fluid wall just behind an air region (or cavity) enclosed by the separating shear layers from the upstream cylinder. The shock wave may consolidate the cavity shape so as to keep it symmetrical with respect to the wake axis against the abundant disturbances around the cavity existing under normal conditions, so that no vortex, or only a symmetrical vortex pair with respect to the wake axis, could be generated in the cavity. It is clear that when no vortex is generated, no vortex shedding occurs. However, even if a symmetrical vortex pair is generated in the cavity, the vortex shedding may not occur, for asymmetry of the vortex pair with respect to the wake axis and the subsequent cross-flow through the wake axis are necessary precursors for the alternate vortex shedding, as proposed by Nakagawa (1986). On the other hand, at low Mach number, with insufficient consolidation of the cavity due to the shock wave, the vortex pair in the cavity may become unstable to disturbances. This leads to asymmetry of the vortex pair with respect to the wake axis and the subsequent cross-flow through the wake axis, so that the vortex shedding starts again. It may be worth noting that the downstream oscillating wake may strengthen the vortex shedding from the cylinder when the oscillation frequency coincides with the vortex-shedding frequency, but this is not necessary for initiating the vortex shedding.

## 5. Conclusions

(i) The regular periodic vortex shedding is present, irrespective of the appearance of shock waves around the square cylinder. The shape of the vortices is, however, deformed by the shock waves and each vortex centre becomes non-uniform while the vortex passes through the gap between the upper and lower shock waves.

(ii) Weak shock waves around the square cylinder do not alter the Strouhal number, but strong shock waves weaken the vortex shedding and increase the Strouhal number suddenly.

(iii) Acoustic waves have been recorded by the Mach–Zehnder interferometer when the Mach number is close to the critical value. The acoustic waves are generated most strongly at the instant when the vortex hits the foot of shock waves formed above and below the vortex formation region.

From the present work and that of Okajima (1982), it is suggested that the Strouhal number of alternating vortices shed from a square cylinder can be estimated to be about 0.13 in the Reynolds number range between $10^2$ and $3.4 \times 10^5$.

This work is supported partly by the Minna–James–Heinemann Foundation, Hannover, Federal Republic of Germany. I would like to express my thanks to the Foundation for the provision of a Fellowship.

I would like to thank Professor Dr E. A. Müller, the Director of the Max-Planck-Institut für Strömungsforschung for the warmest hospitality and for providing me with an opportunity to conduct the present work.

I am grateful to Dr G. E. A. Meier, Dr R. Timm, Mr H.-A. Lent, Mr P. Koperski and Mr D. Perkaus for their permanent assistance during the experiments.

I would like to express my thanks to Professor D. G. Crighton of the University of Cambridge and three anonymous referees for criticisms of the original manuscript and substantial improvements.

## REFERENCES

Bearman, P. W. & Trueman, D. M. 1972 An investigation of the flow around rectangular cylinders. *Aero. Q.* **23**, 229–237.

Bénard, H. 1908 Formation de centres de giration à l'arrière d'un obstacle en mouvement. *C.R. Acad. Sci. Paris* **147**, 839–842.

Dyment, A. 1982 Vortices following two-dimensional separation. In *Vortex Motion* (ed. H. G. Hornung & E. A. Müller), pp. 18–30. Vieweg.

Ericsson, L. & Reding, J. P. 1979 Criterion for vortex periodicity in cylinder wakes. *AIAA J.* **17**, 1012–1013.

Gerrard, J. H. 1966 The mechanics of the formation region of vortices behind bluff bodies. *J. Fluid Mech.* **25**, 401–413.

Kármán, Th. von 1911 Über den Mechanismus des Widerstandes, den ein bewegter Körper in einer Flüssigkeit erfährt. *Nachr. Ges. Wiss. Göttingen*, Math. Phys. Klasse. 509–517.

Kármán, Th. von 1912 Über den Mechanismus des Widerstandes, den ein bewegter Körper in einer Flüssigkeit erfährt. *Nachr. Ges. Wiss. Göttingen*, Math. Phys. Klasse. 547–556.

Lee, B. E. 1975 The effect of turbulence on the surface pressure field of a square prism. *J. Fluid Mech.* **69**, 263–282.

Liepmann, H. W. & Roshko, A. 1957 *Elements of Gas Dynamics*, pp. 164–190. John Wiley.

Mallock, A. 1907 On the resistance of air. *Proc. R. Soc. Lond.* A **79**, 262–273.

Nakagawa, T. 1986 A formation mechanism of alternating vortices behind a circular cylinder at high Reynolds number. *J. Wind Engng Indust. Aero.* **25**, 113–129.

NAKAMURA, Y. & OHYA, Y. 1986 Vortex shedding from square prisms in smooth and turbulent flows. *J. Fluid Mech.* **164**, 77–89.

NASH, J. F., QUINCEY, V. G. & CALLINAN, J. 1963 Experiments on two-dimensional base flow at subsonic and transonic speeds. *A.R.C. Reports and Memoranda* no. 3427.

NAUMANN, A. & PFEIFFER, H. 1958 Versuche an Wirbelstraßen hinter Zylindern bei hohen Geschwindigkeiten. Forschungsberichte des Wirtschafts-und Verkehrsministeriums Nordrhein-Westfalen, no. 493.

OKAJIMA, A. 1982 Strouhal numbers of rectangular cylinders. *J. Fluid Mech.* **123**, 379–398.

RAYLEIGH, L. 1915 Aeolian tones. *Phil. Mag.* S6, **29**, 433–444.

ROSHKO, A. 1961 Experiments on the flow past a circular cylinder at very high Reynolds number. *J. Fluid Mech.* **10**, 345–356.

THOMANN, H. 1959 Measurements of the recovery temperature in wake of a cylinder and of a wedge at Mach numbers between 0.5 and 3. *The Aeronautical Research Institute of Sweden, Report* 84.